Key Points:
- We determine the 1 in 10, 1 in 50, and 1 in 100 year SURF plate currents in medium Earth orbit
- The 1 in 10 year middle plate current decreases with increasing L^* ranging from 0.4 pA/cm^2 at L^*=4.75 to 0.01 pA/cm^2 at L^*=7.0
- The 1 in 100 year middle plate current is a factor of 1.2 to 2.7 larger than the corresponding 1 in 10 year event

Extreme internal charging currents in medium Earth orbit: Analysis of SURF plate currents on Giove-A

Nigel P. Meredith[1], Richard B. Horne[1], John D. Isles[1], Keith A. Ryden[2], Alex D. P. Hands[2], and Daniel Heynderickx[3]

[1]British Antarctic Survey, Natural Environment Research Council, Cambridge, UK, [2]Surrey Space Centre, University of Surrey, Guildford, UK, [3]DHC Consultancy, Leuven, Belgium

Abstract Relativistic electrons can penetrate spacecraft shielding and can damage satellite components. Spacecraft in medium Earth orbit pass through the heart of the outer radiation belt and may be exposed to large fluxes of relativistic electrons, particularly during extreme space weather events. In this study we perform an extreme value analysis of the daily average internal charging currents at three different shielding depths in medium Earth orbit as a function of L^* and along the orbit path. We use data from the SURF instrument on board the European Space Agency's Giove-A spacecraft from December 2005 to January 2016. The top, middle, and bottom plates of this instrument respond to electrons with energies >500 keV, >700 keV, and >1.1 MeV, respectively. The 1 in 10 year daily average top plate current decreases with increasing L^* ranging from 1.0 pA cm^{-2} at L^* = 4.75 to 0.03 pA cm^{-2} at L^*=7.0. The 1 in 100 year daily average top plate current is a factor of 1.2 to 1.8 larger than the corresponding 1 in 10 year current. The 1 in 10 year daily average middle and bottom plate currents also decrease with increasing L^* ranging from 0.4 pA cm^{-2} at L^* = 4.75 to 0.01 pA cm^{-2} at L^*=7.0. The 1 in 100 year daily average middle and bottom plate currents are a factor of 1.2 to 2.7 larger than the corresponding 1 in 10 year currents. Averaged along the orbit path the 1 in 10 year daily average top, middle, and bottom plate currents are 0.22, 0.094, and 0.094 pA cm^{-2}, respectively.

1. Introduction

Relativistic electrons cause internal charging and are a well-known space weather hazard. These so-called "killer" electrons penetrate through spacecraft shielding and may embed themselves in insulators and ungrounded conductors. This charge can accumulate over time resulting in the buildup of high electric fields which may exceed that required for breakdown leading to an internal electrostatic discharge [*Frederickson et al.*, 1991; *Rodgers and Ryden*, 2001]. Such discharges can cause an electronic circuit upset, damage components and, in rare cases, may even cause serious harm to a satellite [e.g., *Koons and Fennel*, 2006]. Indeed, several studies have shown a significant correlation between satellite anomalies and the *E* >2 MeV relativistic electron flux [*Wrenn*, 1995; *Wrenn et al.*, 2002; *Iucci et al.*, 2005].

Relativistic electrons in the Earth's radiation belts occupy two distinct regions. The inner radiation belt, which lies in the approximate range $1.1 < L^* < 2.0$, is relatively stable except during the most intense geomagnetic storms [*Baker et al.*, 2007]. In sharp contrast, the outer radiation belt, which lies in the approximate range $3.0 < L^* < 7.0$, is highly dynamic with fluxes varying by orders of magnitude on a variety of timescales ranging from minutes to tens of days [e.g., *Blake et al.*, 1992; *Baker et al.*, 1994]. The location of the peak of the flux of relativistic electrons in the outer radiation belt is also highly variable, typically lying in the range $3.2 < L^* < 5.5$ [e.g., *Meredith et al.*, 2003].

Global Navigation Satellite Systems (GNSS) such as the U.S. Global Positioning System, the Russian GLONASS system, the developing European Galileo navigation system, and the developing Chinese COMPASS system operate in medium Earth orbit (MEO) at altitudes between 19,000 and 24,000 km. They all pass through the heart of the outer radiation belt where they may be exposed to large fluxes of relativistic electrons. GNSS-enabled devices are used ubiquitously around the globe for positioning and timing information. For example, in 2014 there were 3.6 billion GNSS devices in use and this is forecast to rise to 7 billion by 2019, equivalent to one device per person on the planet [*Global Navigation Satellite Systems Market Report*, 2015]. In 2013 the global market for GNSS products was 175 billion Euros, and this is set to rise to an estimated

237 billion Euros by 2020 [http://europa.eu/rapid/press-release_MEMO-15-4711_en.htm], illustrating the importance of this sector to the economy. It is, therefore, important to understand the environment encountered by satellites in GNSS type orbits and, in particular, the extremes of this environment to be able to better protect space assets operating in this region.

Europe is committed to running its own GNSS system called Galileo. The first test satellite, Giove-A, was launched in 2005 to test technology in orbit for the Galileo navigation system and to claim the frequencies allocated to Galileo by the International Telecommunications Union. There are currently 12 operational satellites in the developing constellation, with European Space Agency expecting to start services by the end of 2016. When fully operational, there will be 30 satellites in MEO, with 10 satellites spread in three different orbital planes inclined at 56° to the equator to ensure global coverage.

Satellites undergoing electric orbit raising also pass through the heart of the outer radiation belt. Electric orbit raising is a novel method of launching satellites that greatly reduces the cost of placing a satellite in geosynchronous orbit. After a traditional launch the satellite undergoes gradual orbit raising via electric propulsion that may take 200 days to raise the orbit from a geosynchronous transfer orbit to geostationary orbit. However, during orbit raising the satellite spends an appreciable proportion of the time in the heart of the outer radiation belt where it will experience a much larger flux of relativistic electrons than would be encountered at geosynchronous orbit. For example, a recent study has estimated that during orbit raising a spacecraft may typically experience a dose equivalent to 6.7 years at geosynchronous orbit or typically half the design lifetime [*Horne and Pitchford*, 2015]. During extreme conditions the dose could be even larger. Better understanding of the extremes of the MEO environment will enable a better assessment of the impact of an extreme event on orbit raising and the resulting life expectancy of the satellite.

In order to better understand the effects of relativistic electrons on satellite components it is useful to directly measure the internal charging currents that penetrate satellite materials. In practice, this is achieved by measuring the internal charging rates at typical shielding depths. These small currents, which are of the order of fA cm^{-2} to pA cm^{-2}, constitute the primary space weather input to the internal charging process and can be directly compared with engineering standards to see whether critical levels are being exceeded and to assess satellite vulnerability. Instruments that measure internal charging rates also have the considerable advantage that they are smaller, much less complex, and cheaper to build and launch than scientific instruments designed to measure fluxes [*Ryden et al.*, 1999].

Internal electrostatic discharges occur as the result of a buildup of charge over time. Thus, a critical quantity for the onset of an internal electrostatic discharge is not the instantaneous charging current but rather the electron charge deposition over a given time interval [*Frederickson et al.*, 1991]. Observations from the CRRES spacecraft showed that few, if any, internal discharges occurred for an average current of 0.1 pA cm^{-2} over a 10 h period [*Frederickson et al.*, 1992]. This figure for the charging current has been used for design guidelines by both NASA [*NASA-HDBK-4002A*, 2011] and the European Centre for Space Standardisation (ECSS) [*ECSS-E-ST-20-06C*, 2008], although a 24 h period rather than a 10 h period is often used [*Ryden et al.*, 2015]. However, the amount of charge accumulated in any given time period also depends on the ability of the material to retain the charge and is thus material dependent. For example, in a recent study using a one-dimensional charging model, *Bodeau* [2010] demonstrated that average currents that are up to 2 orders of magnitude lower than the design guidelines can potentially be a threat for some extremely insulating materials, so long as the currents persist for very long periods.

The current life expectancy of a modern GNSS satellite is 10 to 15 years. Satellite engineers and operators thus require realistic estimates of the largest daily average internal charging currents that may occur on these and longer timescales. Such estimates are needed both to determine the likely impact of an extreme event on GNSS satellites and to improve the resilience of future satellites. The estimates are also of interest to the satellite insurers who require the information on the likely magnitude of an extreme event to help them evaluate potential disaster scenarios.

In this study we used 10 years of data from the SURF detector on board the Giove-A satellite to determine the 1 in 10, 1 in 50, and 1 in 100 year daily average plate currents in MEO. Specifically, we used the top, middle, and bottom plate current data from 29 December 2005 to 5 January 2016. We sorted it by satellite location and calculated the daily average plate current for each of the three plates as a function of L^* and time. We then determined the number of times the daily average plate currents exceeded selected thresholds and

computed probability distribution functions for each plate as a function of L^*. We then conducted extreme value analyses to determine the 1 in 10, 1 in 50, and 1 in 100 year internal charging currents in MEO for each plate as a function of L^*. To compare with engineering design standards we repeated the analysis for each plate using the daily average plate current averaged along the orbit path. The instrumentation and data analysis are described in section 2, and the probability distributions are presented in section 3. The extreme value analysis is introduced in section 4 and the results presented in section 5. Finally, the results are discussed and the conclusions presented in sections 6 and 7, respectively.

2. Instrumentation and Data Analysis

The data used in this study were collected by the SURF detector within the Merlin radiation monitoring instrument on board the European Space Agency's Giove-A satellite. Giove-A was launched on 28 December 2005. The satellite was placed into a circular medium Earth orbit at an altitude of 23,300 km with an inclination of 56° and an orbital period of 14 h. The original mission design lifetime was 27 months, but this has been greatly exceeded and, over 10 years later, the satellite continues to acquire good quality data.

The SURF detector consists of three aluminum collector plates mounted in a stack within a Faraday cage [*Ryden et al.*, 2008]. The top plate, which is 0.5 mm thick, is located under 0.5 mm aluminum equivalent slab shielding. The middle plate, which is also 0.5 mm thick, is located under 1.0 mm aluminum equivalent slab shielding. The bottom plate, which is 1 mm thick, is located under 1.5 mm aluminum equivalent slab shielding. Each of the three collector plates is connected to an electrometer to measure the deposited current. An image of the main detector board and a diagram showing the general configuration of the shielded plates are shown in *Ryden et al.* [2008]. The SURF shielding and absorber plate thickness configuration were selected to be representative of some realistic spacecraft design configurations, but many different shielding/absorber combinations arise in reality. Our analysis of internal charging currents (sections 3 and 4) is restricted to the SURF plate configurations only.

SURF measures charging currents regardless of the cause. However, it has been shown that protons have negligible effects on the currents measured even in major solar proton events [*Ryden et al.*, 2008]. Unlike particle-counting instruments "dead time" does not arise, and thus, no corrections for dead time are required. Based on detailed Monte Carlo radiation transport of the instrument geometry it has been shown that the top plate responds to electrons above 500 keV with a peak response between 700 and 900 keV [*Taylor et al.*, 2009]. The middle plate responds to electrons above 700 keV with a peak response between 1.1 and 1.4 MeV. The bottom plate responds to electrons above 1.1 MeV with a peak response between 1.6 and 2.1 MeV.

The SURF plate current densities in units of pA cm^{-2} are recorded at a 5 min time resolution. In the interests of brevity we refer to the plate current densities as plate currents throughout the text. High and low gain currents are supplied for each plate for each time step. The high gain values give higher accuracy but saturate at 0.514 pA cm^{-2}. We therefore used the high gain values for high gain plate currents below 0.514 pA cm^{-2} and use the low gain plate currents when the high gain plate current exceeds 0.514 pA cm^{-2}.

From the database we determined the daily average plate current for each plate for 10 evenly spaced L^* values from $L^* = 4.75$ to $L^*=7.00$. On any given traverse of the outer radiation belt we determined the plate currents at the selected L^* values by linear interpolation using the plate currents measured at the nearest L^* values either side of the selected L^* value. On any given day this typically yielded seven data points for each plate at each L^* value. Overall, this analysis resulted in ~3025 daily average values at each L^*, corresponding to 8.3 years of good quality operational data. The magnetic coordinate L^* was calculated using the UNILIB software library (http://www.mag-unilib.eu/), adopting the International Geomagnetic Reference Field at the start of the appropriate year together with the Olson-Pfitzer quiet time model [*Olson and Pfitzer*, 1977]. The approximate relationship between L^* and absolute magnetic latitude, $|\lambda_m|$, is shown in Table 1, showing that larger values of L^* are sampled at higher magnetic latitudes. We also calculated the daily average plate currents for each of the plates averaged along the orbit path to compare with engineering design standards. To ensure good coverage we only calculated the daily average plate currents along the orbit path for days with >50% coverage. This resulted in 2758 daily average values for each plate corresponding to 7.6 years of good quality operational data. To help assess the satellite environment at any given time we downloaded and stored the geomagnetic indices and solar wind parameters at a 1 h resolution.

Table 1. Relationship Between L^*, $|\lambda_m|$, and Internal Charging Current Correction Factor for the Giove-A Orbit

| L^*	$|\lambda_m|$ (°)	Correction Factor
4.75	6.0 ± 3.1	1.05
5.00	14.0 ± 2.1	1.23
5.25	19.0 ± 1.6	1.42
5.50	22.4 ± 1.5	1.62
5.75	25.3 ± 1.4	1.83
6.00	27.8 ± 1.5	2.04
6.25	29.9 ± 1.6	2.26
6.50	31.8 ± 1.6	2.49
6.75	33.5 ± 1.8	2.73
7.00	35.0 ± 1.9	2.97

3. Statistics

We first plotted the daily average plate currents as a function of time for selected L^* values for each plate to make sure that there were no outliers in the data. Figure 1 shows a summary plot for 2015, containing a number of plate current intensifications due to high-speed solar wind streams. To put the data in context the plots also show the GOES $E > 2$ MeV electron flux together with relevant solar wind parameters and geophysical indices. From top to bottom the panels show the GOES $E > 2$ MeV electron flux at a 5 min time resolution, the daily average SURF plate currents for $L^* = 6.0$, 5.5, 5.0, and 4.75, the solar wind speed and IMF B_z, the *Dst* index (color coded) and solar wind pressure, and the *Kp* (color coded) and *AE* indices. In the panels showing the SURF plate currents the symbols representing the top, middle, and bottom plate currents are coded black, blue, and red, respectively. The asterisks in the top two panels represent days with anomalies attributed to internal charging, determined from 37 operational satellites in geosynchronous orbit (D. Pitchford, personal communication, 2016).

This period is characterized by a number of plate current intensifications caused by recurrent high-speed solar wind streams. Indeed, some of the largest plate currents in the 10 year history of the mission were observed during the year. For example, on 9 October 2015 the daily average top, middle, and bottom plate currents at $L^* = 4.75$ were 0.8, 0.31, and 0.27 pA cm^{-2}, respectively, all lying in the top 10 events at this location (Table 2). We produced monthly and yearly summary plots in the same format and inspected them for outliers. The data from each of the plates were confirmed to be very clean and no outliers were found.

In Tables 2 and 3 we tabulate the top 10 daily average top, middle, and bottom plate currents observed at $L^* = 4.75$ and $L^* = 6.0$, respectively. The largest daily average top plate current observed at $L^* = 4.75$, near the lowest L^* value sampled by Giove-A, was 1.22 pA cm^{-2} on 6 April 2010. The largest daily average middle and bottom plate currents at $L^* = 4.75$ were observed 2 days later and were a factor of ~3 lower at 0.43 and 0.48 pA cm^{-2}, respectively. The largest daily average top, middle, and bottom plate currents at $L^* = 6.0$, on field lines that map out close to geosynchronous orbit, were about a factor of 10 lower for each of the plates, respectively, and all occurred on 10 April 2010.

We then determined the number of times the internal charging currents exceeded selected thresholds as a function of L^* for each plate. The results are presented in Table 4. Large top plate currents occurred most frequently in the region $4.75 < L^* < 6.0$. The number of times the daily average top plate current exceeded 0.02 pA cm^{-2} reached a maximum value of 2233 at $L^* = 5.0$. For the middle and bottom plates the largest currents occurred most frequently in the region $4.75 < L^* < 5.5$. Here the peak in the number of times the daily average plate currents exceeded 0.02 pA cm^{-2} occurred closer at $L^* = 4.75$.

The distributions of the daily average top plate currents for the selected L^* values are shown in Figure 2a. The top plate currents cover over 2 orders of magnitude and range from 0.005 to 1.2 pA cm^{-2}. The largest observed top plate current ranges from 1.2 pA cm^{-2} at $L^* = 4.75$ to 0.04 pA cm^{-2} at $L^* = 7$. The plate currents corresponding to selected exceedable probabilities are shown as a function of L^* in Figure 2d. The 0.1% exceedance level decreases with L^* ranging from 0.83 pA cm^{-2} at $L^* = 4.75$ to 0.028 pA cm^{-2} at $L^* = 7.0$.
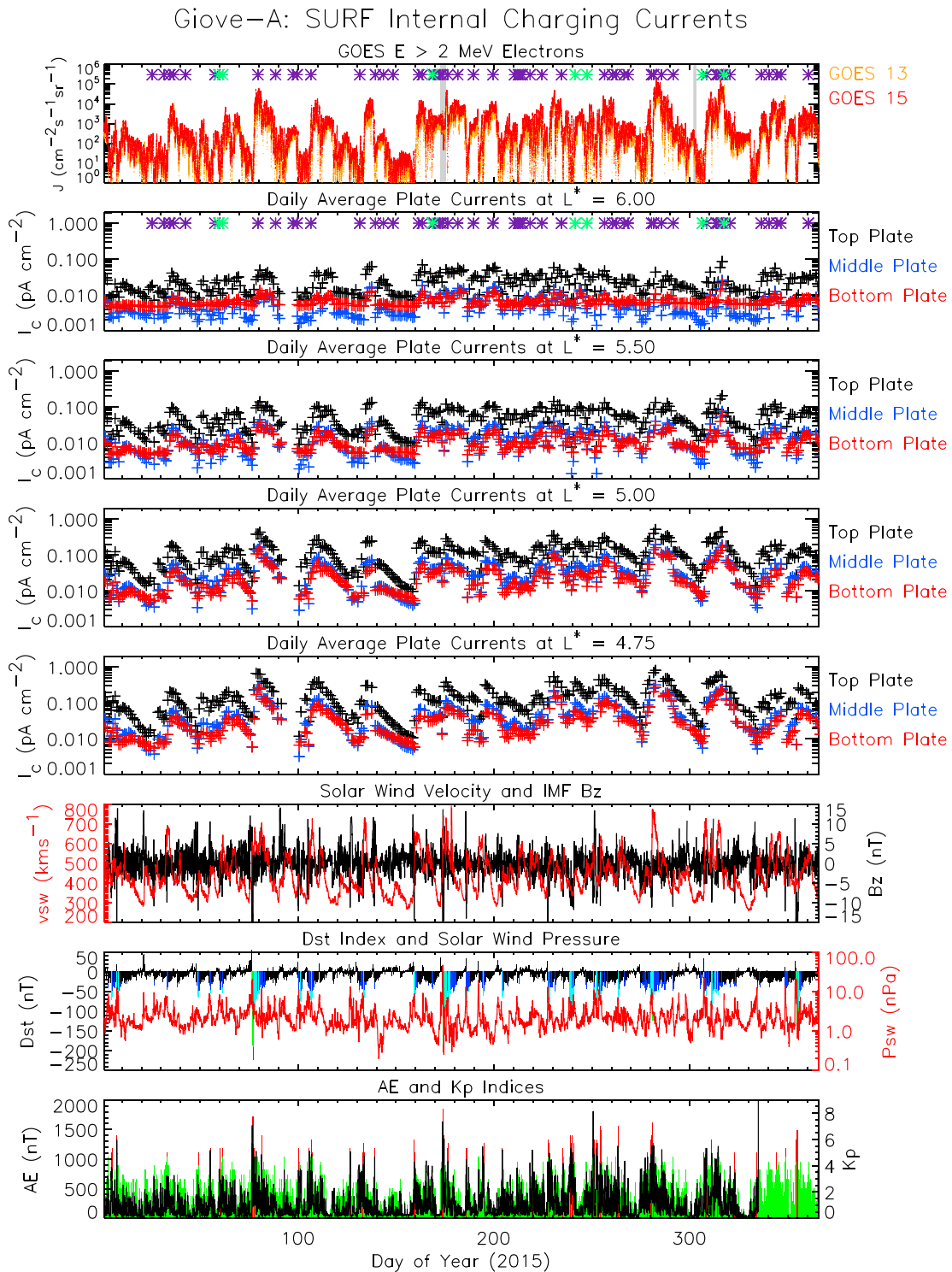
Figure 1. Summary plot of the SURF plate currents from 2015. From top to bottom the panels show the GOES $E > 2$ MeV electron flux, the SURF plate currents for $L^* = 6.0$, 5.5, 5.0, and 4.75, the solar wind speed and IMF B_z, the Dst index (color coded) and solar wind pressure, and the Kp (color coded) and AE indices. In the panels showing the SURF plate currents the symbols representing the top, middle, and bottom plate currents are coded black, blue, and red, respectively. In the top two panels the asterisks represent days with one (purple) or two (green) satellite anomalies as determined from 37 satellites in geosynchronous orbit.

Table 2. Largest Daily Average Top, Middle, and Bottom Plate Currents Observed at $L^* = 4.75$

Top Plate		Middle Plate		Bottom Plate	
Current		Current		Current	
(pA cm^{-2})	Date	(pA cm^{-2})	Date	(pA cm^{-2})	Date
1.22	6 Apr 2010	0.43	8 Apr 2010	0.48	8 Apr 2010
0.83	16 Dec 2006	0.40	6 Apr 2010	0.43	9 Apr 2010
0.83	15 Dec 2006	0.37	9 Apr 2010	0.38	10 Apr 2010
0.81	8 Apr 2010	0.33	10 Apr 2010	0.32	17 Apr 2006
0.80	9 Oct 2015	0.33	16 Dec 2006	0.30	6 Apr 2010
0.70	8 Oct 2015	0.32	17 Apr 2006	0.29	11 Apr 2010
0.69	15 Apr 2006	0.31	9 Oct 2015	0.29	16 Apr 2006
0.67	19 Mar 2015	0.30	16 Apr 2006	0.27	18 Apr 2006
0.66	17 Apr 2006	0.29	15 Dec 2006	0.27	9 Oct 2015
0.66	17 Jul 2012	0.28	15 Apr 2006	0.27	16 Dec 2006

The distributions of the daily average middle plate currents are shown in Figure 2b in the same format as Figure 2a. The middle plate currents cover over 2 orders of magnitude and range from 0.001 to 0.43 pA cm^{-2}. The largest observed middle plate current ranges from 0.43 pA cm^{-2} at $L^*=4.75$ to 0.01 pA cm^{-2} at $L^*=7$. The plate currents that are exceeded for selected fractions of the time are shown in Figure 2e. The 0.1% exceedance level decreases with L^* ranging from 0.37 pA cm^{-2} at $L^*=4.75$ to 0.0086 pA cm^{-2} at $L^*=7.0$.

The distributions of the daily average bottom plate currents are shown in Figure 2c in the same format as Figure 2a. The bottom plate currents cover over 2 orders of magnitude and range from 0.004 to 0.48 pA cm^{-2}. The largest observed bottom plate current ranges from 0.48 pA cm^{-2} at $L^*=4.75$ to 0.02 pA cm^{-2} at $L^*=7$. The plate currents that are exceeded for selected fractions of the time are shown in Figure 2f. The 0.1% exceedance level is very similar to that obtained for the middle plate, ranging from 0.38 pA cm^{-2} at $L^*=4.75$ to 0.01 pA cm^{-2} at $L^*=7.0$.

The distribution of the daily average plate currents averaged along the orbit path are shown in Figure 3. The top plate currents (Figure 3a) range from 0.003 to 0.2 pA cm^{-2}. The middle plate currents (Figure 3b) cover 2 orders of magnitude and range from 0.001 to 0.1 pA cm^{-2}. The bottom plate currents (Figure 3c) range from 0.003 to 0.1 pA cm^{-2}.

4. Extreme Value Analysis

To determine the 1 in N year plate currents we conducted an extreme value analysis of the daily average top, middle, and bottom plate currents as a function of L^* using the exceedances over a threshold approach described in detail in *Meredith et al.* [2015]. For each plate and L^* we set the threshold at the 1.5% exceedance

Table 3. Largest Daily Average Top, Middle, and Bottom Plate Currents Observed at $L^* = 6.0$

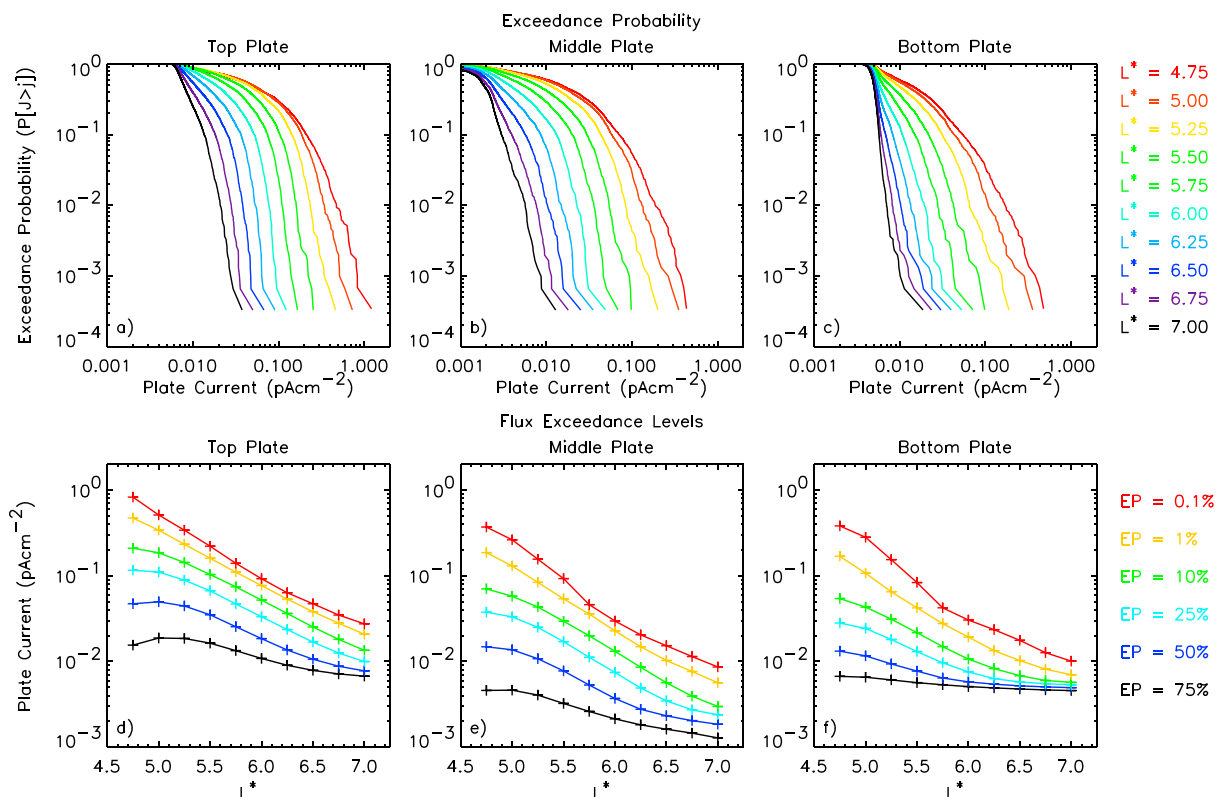| Top Plate		Middle Plate		Bottom Plate	
Current		Current		Current	
(pA cm^{-2})	Date	(pA cm^{-2})	Date	(pA cm^{-2})	Date
0.12	10 Apr 2010	0.049	10 Apr 2010	0.048	10 Apr 2010
0.095	17 Apr 2006	0.031	3 Apr 2008	0.043	3 Apr 2008
0.093	4 Sep 2007	0.030	17 Apr 2006	0.038	11 Apr 2010
0.092	8 Apr 2010	0.029	2 Apr 2008	0.032	2 Apr 2008
0.088	17 Oct 2006	0.029	4 Sep 2007	0.030	19 Apr 2006
0.086	22 Sep 2006	0.028	17 Oct 2006	0.029	31 Mar 2008
0.086	1 Oct 2007	0.028	11 Apr 2010	0.029	8 Apr 2010
0.085	12 Nov 2015	0.028	4 Mar 2008	0.027	30 May 2007
0.085	11 Apr 2008	0.027	31 Mar 2008	0.027	4 Mar 2008
0.084	13 Aug 2008	0.027	30 May 2007	0.027	21 Mar 2012

Table 4. Number of Times the Daily Average Plate Current Exceeds Certain Thresholds

	Top Plate			Middle Plate			Bottom Plate		
L^*	0.02 (pA cm^{-2})	0.05 (pA cm^{-2})	0.1 (pA cm^{-2})	0.02 (pA cm^{-2})	0.05 (pA cm^{-2})	0.1 (pA cm^{-2})	0.02 (pA cm^{-2})	0.05 (pA cm^{-2})	0.1 (pA cm^2)
4.75	2052	1399	860	1221	491	155	1056	320	99
5.00	2233	1504	851	1167	417	87	947	235	42
5.25	2218	1383	656	923	214	12	662	101	8
5.50	2057	1091	330	624	47	0	352	14	0
5.75	1801	692	72	300	2	0	115	1	0
6.00	1407	333	1	52	0	0	28	1	0
6.25	950	53	0	5	0	0	4	0	0
6.50	537	1	0	1	0	0	1	0	0
6.75	214	1	0	0	0	0	1	0	0
7.00	40	0	0	0	0	0	0	0	0

level for the given plate and L^* and declustered the data using the same empirical rule as *Meredith et al.* [2015]. We then fitted the generalized Pareto distribution (GPD) [*Picklands*, 1975; *Coles*, 2001] to the cluster maxima as a function of L^* for each plate using the ismev library routine gpd.fit [*Heffernan et al.*, 2014] provided in the R statistical package [*R Development Core Team*, 2008]. The GPD may be written as follows:
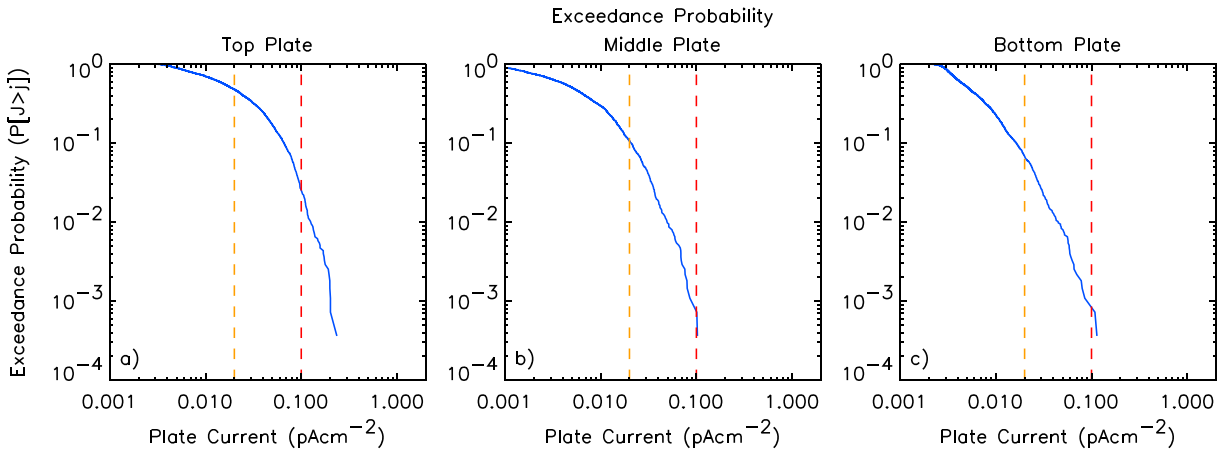
$$G(y) = 1 - \left(1 + \frac{\xi y}{\sigma}\right)^{-\frac{1}{\xi}} \qquad (1)$$

Figure 2. Plots of the exceedance probabilities for the daily average (a) top plate, (b) middle plate, and (c) bottom plate currents at selected L^* values and plate current exceedance levels as a function of L^* for the (d) top plate, (e) middle plate, and (f) bottom plate currents.

Giove−A SURF Daily Average Plate Currents Along Orbit Path
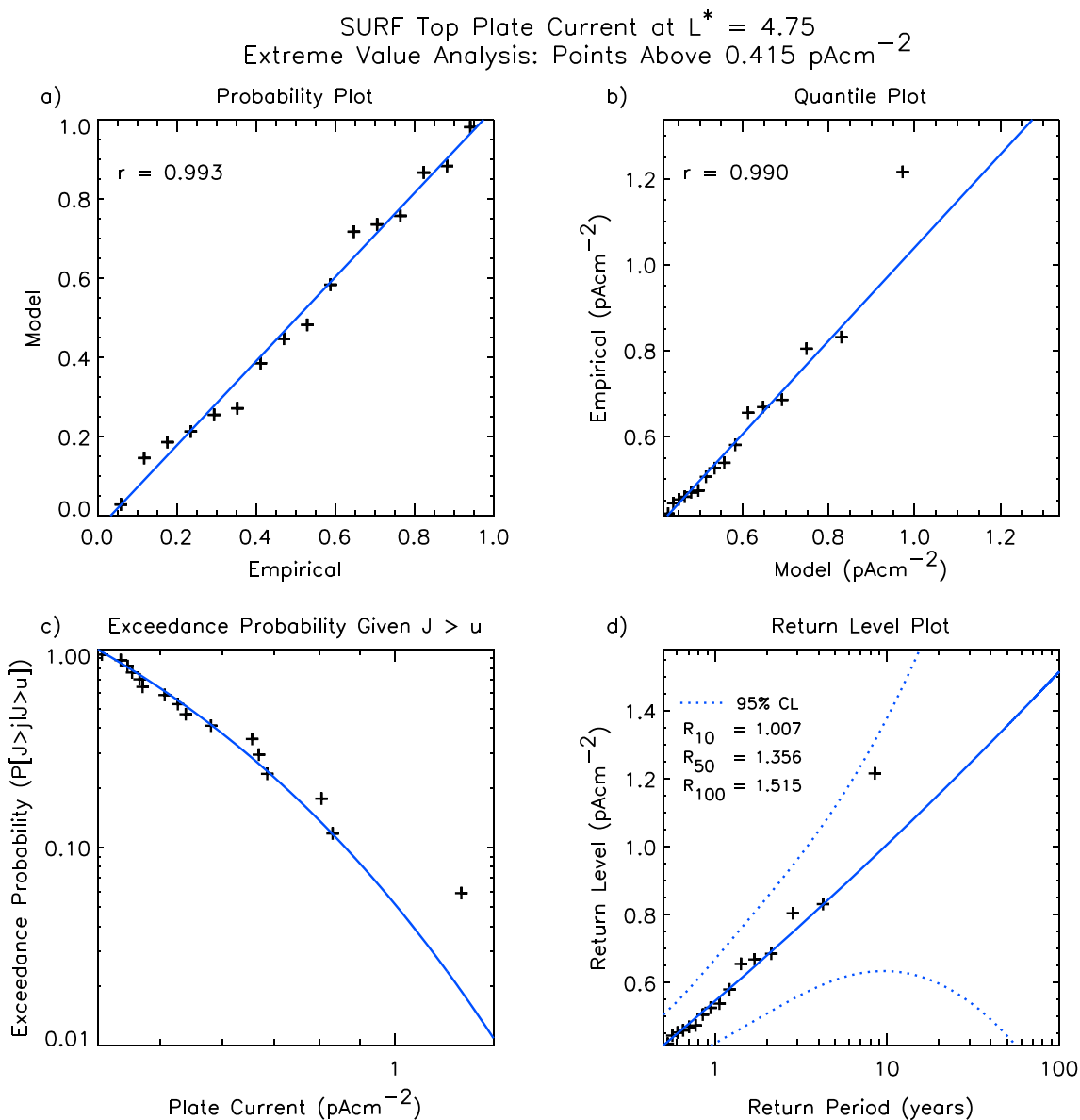
Exceedance Probability

Figure 3. Plots of the exceedance probabilities for the daily average (a) top plate, (b) middle plate, and (c) bottom plate currents along the orbit path. The orange and red dashed lines denote the 0.02 and 0.1 pA cm^{-2} thresholds used as engineering standards.

where $y = (x − u)$ are the exceedances, x are the cluster maxima above the chosen threshold, u, ξ is the shape parameter, and σ the scale parameter [*Coles*, 2001]. The sign of the shape parameter provides important information on the behavior of the tail of the distribution. If ξ is positive the distribution has no upper limit, whereas if ξ is negative the distribution has an upper bound. The level, x_N, which is exceeded on average once every N years may be expressed in terms of ξ and σ as

$$x_N = u + \frac{\sigma}{\xi}\left(\left(Nn_d n_c / n_{\text{tot}}\right)^{\xi} - 1\right) \tag{2}$$
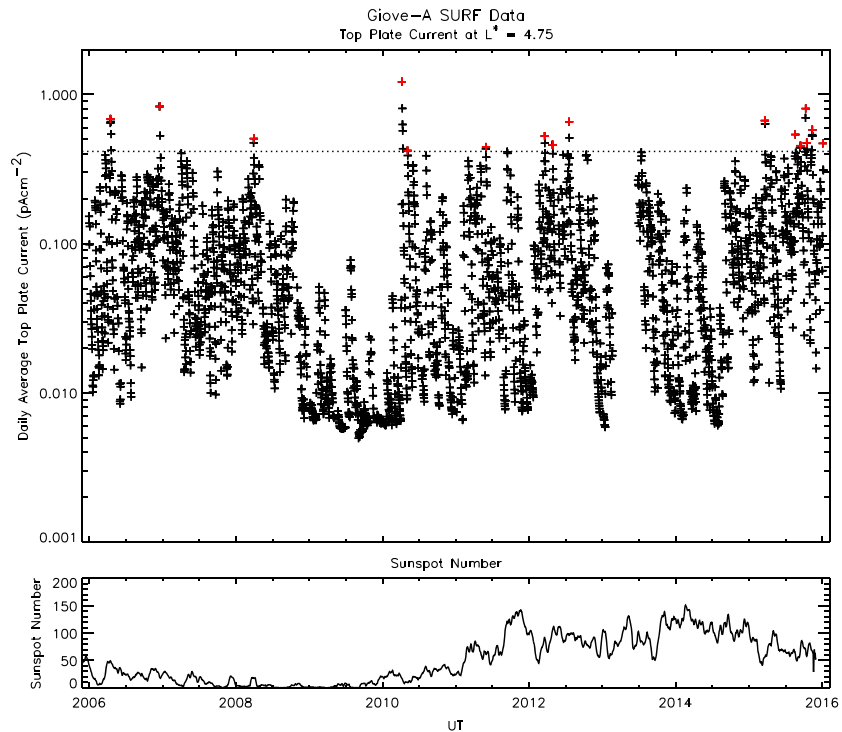
Figure 4. Plot of the daily average top plate currents as a function of UT time at $L^* = 4.75$. (top) The 0.1% exceedance level, chosen as the threshold for the extreme value analysis, is shown as a dotted line and the cluster maxima are coded red. (bottom) Trace of the sunspot number as a function of universal time.

Figure 5. Extreme value analysis for the daily average top plate currents at $L^* = 4.75$. (a) Probability plot, (b) quantile plot, (c) the exceedance probability given $J > u$, and (d) the return level plot.

where n_c is the number of clusters, n_{tot} is the total number of data points, and $n_d = 365.25$ is the average number of days in any given year [*Coles*, 2001].

5. Results

To illustrate the technique we first consider the top plate current at $L^* = 4.75$. Figure 4 shows the daily average top plate current as a function of universal time (UT) (Figure 4, top), together with a trace of the sunspot number (Figure 4, bottom). The 1.5% exceedance level of 0.415 pA cm^{-2} is shown as the dotted line and the individual cluster maxima are colored red. The daily average top plate current may exceed the threshold during most phases of the solar cycle, although there is a distinct minimum in the top plate currents between 2008 and 2010.

For the top plate currents at $L^* = 4.75$ the maximum likelihood estimates of the scale and shape parameters are (0.19 ± 0.07) and 0.04 ± 0.29, respectively. The shape parameter is close to zero making it difficult to infer whether or not the currents tend to a limit. The probability plot, which displays the modeled probability
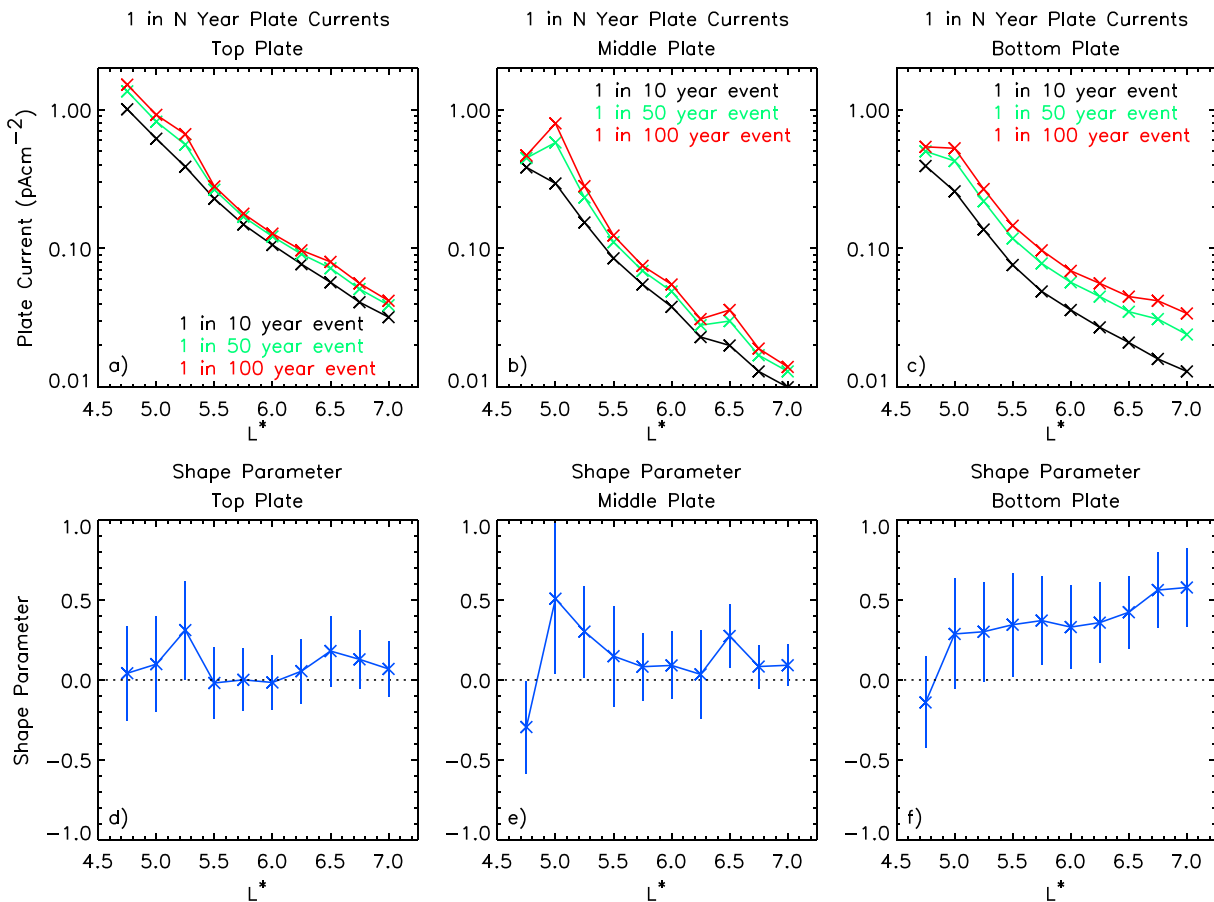
Figure 6. Plots of the 1 in N year daily average plate currents as a function of L^* for $N=10$ (black), 50 (green), and 100 years (red) for the (a) top plate, (b) middle plate, and (c) bottom plate currents and the shape parameter as a function of L^* for the (d) top plate, (e) middle plate, and (f) bottom plate currents.

against the empirical probability, for the cluster maxima of the daily average top plate currents is shown in Figure 5a. The best fit straight line to the data points is shown in blue and has a correlation coefficient of 0.993. The quantile plot, which displays the empirical quantiles against the modeled quantiles, for the cluster maxima of the daily average top plate currents is shown in Figure 5b. The best fit straight line is again shown in blue and has a correlation coefficient of 0.990. Both fits are approximately linear suggesting that the generalized Pareto model is a good method for modeling the exceedances [e.g., *Coles*, 2001].

The exceedance probability of the cluster maxima above the threshold value of 0.415 pA cm^{-2}, $(P[J > j|J > u])$, is shown in Figure 5c (black symbols), together with the maximum likelihood fit (blue line). The plate current that is exceeded on average once every N years is shown as a function of N for the declustered top plate currents in Figure 5d. The solid blue line represents the 1 in N year return level determined from equation (2) and the symbols represent the experimental return levels. The blue dotted lines represent the 95% confidence interval of the 1 in N year return level. This type of plot is known as a return level plot. The 1 in 10, 1 in 50, and 1 in 100 year daily average top plate currents at $L^*=4.75$ are 1.0, 1.4, and 1.5 pA cm^{-2}.

We repeated the analysis of the daily average top plate currents for other values of L^* and determined the corresponding 1 in N year events. Figure 6a shows the results for $N=10$, 50, and 100 years. The 1 in 10 year event (black line) decreases with increasing L^* and ranges from 1.0 pA cm^{-2} at $L^*=4.75$ to 0.03 pA cm^{-2} at $L^*=7.0$. The 1 in 100 year event (red line) exhibits a similar trend lying in the range 1.5 to 0.04 pA cm^{-2} and is a factor of 1.2 to 1.8 larger than the corresponding 1 in 10 year event. Figure 6d shows the shape parameter for the top plate currents as a function of L^*. The shape parameter is mostly positive, but the error bars are large making it difficult to conclude whether or not there is an upper limit to the top plate currents.

We repeated the analysis for the daily average middle plate currents. Figure 6b shows the resulting 1 in N year event as a function of L^* for $N=10$, 50, and 100 years. The 1 in 10 year event (black line) also maximises at

$L^* = 4.75$ and decreases with increasing L^* ranging from 0.4 pA cm^{-2} at $L^* = 4.75$ to 0.01 pA cm^{-2} at $L^* = 7.0$. The 1 in 100 year event (red line) is a factor of 1.2 to 2.7 larger than the corresponding 1 in 10 year event. Figure 6e shows the shape parameter for the middle plate currents as a function of L^*. The shape parameter is largely positive, but the error bars include positive and negative values suggesting that more data are required to determine whether the top plate currents are bounded or unbounded.

We then analyzed the daily average bottom plate currents. Figure 6c shows the 1 in N year event as a function of L^* for $N = 10$, 50, and 100 years. The 1 in 10 year daily average bottom plate currents are similar to the 1 in 10 year daily average middle plate currents and range from 0.4 pA cm^{-2} at $L^* = 4.75$ to 0.01 pA cm^{-2} at $L^* = 7.0$. The 1 in 100 year event (red line) is a factor of 1.4 to 2.6 larger than the corresponding 1 in 10 year event. Figure 6f shows the shape parameter for the bottom plate currents as a function of L^*. The shape parameter is mostly positive suggesting that the bottom plate currents do not have an upper limit.

Finally, we performed an extreme value analysis of the daily average plate currents averaged along the orbit path. The 1 in 10, 1 in 50, and 1 in 100 year daily average top plate currents averaged along the orbit path were found to be 0.22, 0.24, and 0.25 pA cm^{-2}. The 1 in 10, 1 in 50, and 1 in 100 year daily average middle plate currents were found to be 0.094, 0.11, and 0.12 pA cm^{-2}. The 1 in 10, 1 in 50, and 1 in 100 year bottom plate currents were very similar to those determined for the daily average middle plate currents being 0.094, 0.12, and 0.13 pA cm^{-2} respectively.

6. Discussion

The nature of the Giove-A orbit is such that higher values of L^* are sampled at higher magnetic latitudes (Table 1). Since electron pitch angle distributions in the outer radiation belt are anisotropic, the flux and hence internal charging current, varies as a function of magnetic latitude. The precise relationship depends on the equatorial pitch angle distribution which in turn depends on many factors such as L^*, local time and magnetic activity. In the absence of this precise information, we assume the same relationship between internal charging current and magnetic latitude as between flux and magnetic latitude in the FLUMIC model [*Wrenn et al.*, 2000; *Rodgers et al.*, 2003], which in turn is based on the work of *Vette* [1991] used in AE8. The correction factors to convert from local to equatorial internal charging currents are tabulated in Table 1 as a function of L^*. For example, Giove-A crosses field lines that map to geosynchronous orbit, corresponding to $L^* = 6.0$, at a magnetic latitude of 27.8 ± 1.5°. Here the measured internal charging currents should be multiplied by a factor of 2 to obtain those that would be obtained by a geosynchronous satellite near the geomagnetic equator.

The largest plate currents for a given 1 in N year event tend to be observed at $L^* = 4.75$. For example, the largest 1 in 10 year daily average middle plate current of 0.38 pA cm^{-2} occurs at $L^* = 4.75$ and is a factor of 10 times larger than the corresponding value of 0.038 pA cm^{-2} at $L^* = 6.0$, on field lines that map out close to geosynchronous orbit. The 1 in 10 year event for the daily average middle plate current averaged along the orbit path is 0.094 pA cm^{-2}, which is a factor of ~2.6 times that at $L^* = 6.0$. Mapping these results to the magnetic equator, using the correction factors in Table 1, the 1 in 10 year middle plate current at $L^* = 4.75$ is a factor of ~5 times larger than that which would be observed at $L^* = 6.0$, near geosynchronous orbit in the magnetic equatorial plane. The 1 in 10 year daily average middle plate current averaged along the orbit path is a factor of ~1.3 times larger than the 1 in 10 year daily average middle plate current which would be observed near geosynchronous orbit in the equatorial plane. The results from all three plates suggest that the 1 in 10 year daily average plate current averaged along the orbit path is similar in magnitude to the 1 in 10 year daily average plate current that would be observed at geosynchronous orbit in the magnetic equatorial plane.

At $L^* = 6.0$, on field lines that map to geosynchronous orbit, we find a factor of ~2 difference between the 1 in 100 and 1 in 10 year plate currents. In contrast, *Meredith et al.* [2015] found a factor of 4 to 5 difference between the 1 in 100 and 1 in 10 year $E > 2$ MeV electron fluxes at geosynchronous orbit. This difference is most likely due to the different electron energy responses of the two instruments. GOES responds to $E > 2$ MeV electrons, whereas the bottom plate of the SURF instrument responds to electrons with energies greater than 1.1 MeV with a peak response between 1.6 and 2.1 MeV. For the top and middle plates, which respond to lower energies, the ratio of the 1 in 100 to 1 in 10 year plate currents at $L^* = 6.0$ are 1.21 and 1.45, respectively. This suggests that the ratio of the 1 in 100 to 1 in 10 year events increases with increasing energy. This effect can be seen in Figure 6—especially for the increase in the ratio between the 1 in 100 year event and the 1 in 10 year event for the middle and bottom plates. These results suggest that the ratio of the 1 in 100 to 1 in 10 year event would be larger for a plate responding to $E > 2$ MeV electrons. Furthermore, *Meredith et al.* [2015]

analyzed ~20 years of data, whereas this study analyzes 10 years of data, biased toward lower geomagnetic activity and, therefore, more likely limited to lower levels of overall variability.

The shape parameter for the top, middle, and bottom plate currents is predominantly positive. However, the error bars are large and often span zero making it difficult to be conclusive for the top and middle plates. The results are more convincing for the bottom plate with most of the error bars remaining in positive territory. This suggests that the bottom plate currents have no upper limit, consistent with previous findings for the flux of $E > 2$ MeV electrons at geosynchronous orbit [*Meredith et al.*, 2015] and the flux of $E > 100$ keV and $E > 300$ keV electrons in low Earth orbit [*Meredith et al.*, 2016]. In contrast, *O'Brien et al.* [2007] found evidence to suggest that outer radiation belt electron fluxes from approximately 450 keV to several MeV have finite upper limits. Further analysis requiring longer time series of data is required to conclusively establish the presence or absence of an upper bound. In reality, a physical process or set of processes is likely to set upper limit, but this is not evident from the analysis presented here.

The amount of geomagnetic activity increased during 2015, largely in association with an increase in the number of recurrent high-speed solar wind streams. The fluxes of relativistic electrons at geosynchronous orbit and the plate currents at $L^* = 6.0$ were also more elevated in the second half of 2015. The number of satellite anomalies thought to be due to internal electrostatic discharge also increased during the year. For example, based on information from 37 operational satellites in geosynchronous orbit, there were 19 such anomalies in the first 160 days of the year and 40 in the next 160 days (D. Pitchford, personal communication, 2016). The days with one anomaly are marked as purple asterisks and the days with two anomalies are marked as green asterisks in Figure 1. Most, but not all, are associated with increased fluxes of relativistic electrons at geosynchronous orbit and increased plate currents at $L^* = 6.0$. More generally, these results demonstrate the use of combining information on satellite anomalies with plate current and flux data in a bid to help determine the cause of any given satellite anomaly. However, since internal charging may be a result of charge accumulated over time [*Bodeau*, 2010], we do not expect a direct one to one relationship between large plate currents and satellite anomalies.

Recurrent high-speed solar wind streams, which are most common during the declining phase of the solar cycle [*Burlaga and Lepping*, 1977; *Gonzalez et al.*, 1999], are associated with coronal holes on the Sun which are long lasting and can survive several solar rotations. Sometimes there can be two high-speed solar wind stream-driven storms per solar rotation resulting in an even shorter time period between events [e.g., *Baker et al.*, 1997]. Individual storms driven by high-speed solar wind streams may increase the flux of relativistic electrons in the outer radiation belt by an order of magnitude or more [e.g., *Baker et al.*, 1994, 1997; *Lam et al.*, 2009]. Since charge accumulated takes time to decay [e.g., *Bodeau*, 2010] recurrent intensifications associated with high-speed solar wind streams can be particularly damaging, especially for materials with long decay time constants, since they are more likely to lead to the buildup of a sufficient amount of charge to trigger an internal electrostatic discharge.

It is interesting to compare the daily average plate currents averaged along the orbit path for each of the plates with the current guidelines on charging current deposition. NASA have devised guidelines on charging current [*NASA-HDBK-4002A*, 2011], notably an average current of 0.1 pA cm^{-2} over a 10 h period, although a 24 h period is also used and we adopt this here (red dashed line in Figure 3). The guidelines assume a current and a time period since it is the accumulated charge that is important for the onset of an internal electrostatic discharge. This threshold is also used in the European ECSS standards [*ECSS-E-ST-20-06C*, 2008]. For dielectrics operating at temperatures less than 25°C the threshold is 0.02 pA cm^{-2} (orange dashed line in Figure 3). The lower threshold is commonly exceeded in all three plates, being exceeded 48%, 11%, and 6.8% of the time for the top, middle, and bottom plates, respectively, consistent with *Ryden et al.* [2015]. The higher threshold is exceeded much less often being exceeded 2.5%, 0.07%, and 0.07% of the time for the top, middle, and bottom plates, respectively. The results of the extreme value analysis suggest that the return period of the 0.1 pA cm^{-2} threshold is 113 days, 16.1 years, and 13.3 years for the top, middle, and bottom plates, respectively.

7. Conclusions

We have conducted an extreme value analysis of the daily average top, middle, and bottom plate currents as a function of L^* from the SURF instrument on Giove-A for the 10 year period from 29 December 2005 to 5 January 2016. Our principle results are as follows:

1. The 1 in 10 year daily average top plate current decreases with increasing L^* ranging from 1.0 pA cm^{-2} at $L^*=4.75$ to 0.03 pA cm^{-2} at $L^*=7.0$.
2. The 1 in 100 year daily average top plate current lies in the range 1.5 to 0.04 pA cm^{-2} and is generally a factor of 1.2 to 1.8 larger than the corresponding 1 in 10 year current.
3. The 1 in 10 year daily average middle plate current also decreases with increasing L^* ranging from 0.4 pA cm^{-2} at $L^*=4.75$ to 0.01 pA cm^{-2} at $L^*=7.0$.
4. The 1 in 100 year daily average middle plate current is a factor of 1.2 to 2.7 larger than the corresponding 1 in 10 year current.
5. The 1 in 10 year daily average bottom plate currents are similar to the 1 in 10 year daily average middle plate currents ranging from 0.4 pA cm^{-2} at $L^*=4.75$ to 0.01 pA cm^{-2} at $L^*=7.0$.
6. The 1 in 100 year daily average bottom plate current is a factor of 1.4 to 2.6 larger than the corresponding 1 in 10 year current.
7. Averaged along the orbit path the 1 in 10 year daily average top, middle, and bottom plate currents are 0.22, 0.094, and 0.094 pA cm^{-2}, respectively.

Our conclusions are based on ∼8 years of good quality data, from a 10 year data set. We thus have to extrapolate far into the tail of the distribution to determine the 1 in 100 year plate currents. To improve our estimates of the 1 in 100 year plate currents a longer time series is required and this is a compelling reason to keep the SURF instrument on Giove-A running for as long as possible. Furthermore, we recommend deployment of more SURF-type sensors since they fill a key gap between the space environment and engineering effects.

References

Baker, D. N., J. B. Blake, L. B. Callis, J. R. Cummings, D. Hovestadt, S. Kanekal, B. Klecker, R. A. Mewaldt, and R. D. Zwickl (1994), Relativistic electron acceleration and decay time scales in the inner and outer radiation belts: SAMPEX, *Geophys. Res. Lett.*, *21*, 409–412.

Baker, D. N., et al. (1997), Recurrent geomagnetic storms and relativistic electron enhancements in the outer magnetosphere: ISTP coordinated measurements, *J. Geophys. Res.*, *102*, 14,141–14,148.

Baker, D. N., S. G. Kanekal, R. B. Horne, N. P. Meredith, and S. A. Glauert (2007), Low-altitude measurements of 2–6 MeV electron trapping lifetimes at $1.5 \leq L \leq 2.5$, *Geophys. Res. Lett.*, *34*, L20110, doi:10.1029/2007GL031007.

Blake, J. B., W. A. Kolasinski, R. W. Fillius, and E. G. Mullen (1992), Injection of electrons and protons with energies of tens of MeV into $L < 3$ on 24 March 1991, *Geophys. Res. Lett.*, *19*(8), 821–824.

Bodeau, M. (2010), High energy electron climatology that supports deep charging risk assessment in GEO, paper AIAA 2010–1608 presented at 48th AIAA Aerospace Sciences Meeting Including the New Horizons Forum and Aerospace Exposition, Orlando, Florida, 4–7 Jan., doi:10.2514/6.2010-1608.

Burlaga, L. F., and R. P. Lepping (1977), The causes of recurrent geomagnetic storms, *Planet. Space Sci.*, *25*, 1151–1160.

Coles, S. (2001), *An Introduction to Statistical Modelling of Extreme Values*, Springer, London.

ECSS-E-ST-20-06C (2008), *Space Engineering: Spacecraft Charging*, ECSS Secretariat, ESA-ESTEC Requirements and Standards Division Noordwijk, Netherlands.

Frederickson, A. R., E. G. Mullen, D. H. Brautigam, K. J. Kerns, and E. G. Holman (1991), Radiation-induced insulator discharge pulses in the CRRES internal discharge monitor satellite experiment, *IEEE Trans. Nucl. Sci.*, *38*, 778–784.

Frederickson, A. R., E. G. Holeman, and E. G. Mullen (1992), Characteristics of spontaneous electron discharging of various insulators in space radiations, *IEEE Trans. Nucl. Sci.*, *39*, 1773–1982.

Global Navigation Satellite Systems Market Report (2015), *Issue 4*, European GNSS Agency, Czech Republic, Prague.

Gonzalez, W. D., B. T. Tsurutani, and A. L. Clua de Gonzalez (1999), Interplanetary origin of geomagnetic storms, *Space Sci. Rev.*, *88*, 529–562.

Heffernan, J. E., A. G. Stephenson, and E. Gilleland (2014), ISMEV: An introduction to statistical modeling of extreme values, version 1.39. [Available at http://www.ral.ucar.edu/ericg/softextreme.php.]

Horne, R. B., and D. Pitchford (2015), Space weather concerns for all-electric propulsion satellites, *Space Weather*, *13*, 430–433, doi:10.1002/2015SW001198.

Iucci, N., et al. (2005), Space weather conditions and spacecraft anomalies in different orbits, *Space Weather*, *3*, S01001, doi:10.1029/2003SW000056.

Lam, M. M., R. B. Horne, N. P. Meredith, and S. A. Glauert (2009), Radiation belt electron flux variability during three CIR-driven geomagnetic storms, *J. Atmos. Sol. Terr. Phys.*, *71*, 1145–1156.

Koons, H. C., and J. F. Fennel (2006), Space weather effects on communications satellites, *Sci. Bull. Int. Union Radio Sci. (URSI)*, *316*, 27–41.

Meredith, N. P., M. Cain, R. B. Horne, R. M. Thorne, D. Summers, and R. R. Anderson (2003), Evidence for chorus-driven electron acceleration to relativistic energies from a survey of geomagnetically disturbed periods, *J. Geophys. Res.*, *108*(A6), 1248, doi:10.1029/2002JA009764.

Meredith, N. P., R. B. Horne, J. D. Isles, and J. V. Rodriguez (2015), Extreme relativistic electron fluxes at geosynchronous orbit: Analysis of GOES $E > 2$ MeV electrons, *Space Weather*, *13*, 170–184, doi:10.1002/2014SW001143.

Meredith, N. P., R. B. Horne, J. D. Isles, and J. C. Green (2016), Extreme energetic electron fluxes in low Earth orbit: Analysis of POES $E > 30$, $E > 100$ and $E > 300$ keV electrons, *Space Weather*, *14*, 136–150, doi:10.1002/2015SW001348.

NASA-HDBK-4002A (2011), *NASA Technical Handbook: Mitigating In-Space Charging Effects—A Guideline*, Natl. Aeronaut. Space Admin., Washington, D. C.

O'Brien, T. P., J. F. Fennell, J. L. Roeder, and G. D. Reeves (2007), Extreme electron fluxes in the outer zone, *Space Weather*, *5*, S01001, doi:10.1029/2006SW000240.

Olson, W. P., and K. Pfitzer (1977), *Magnetospheric Magnetic Field Modelling Annual Scientific Report*, Air Force Off. of Sci. Res., Arlington, Va.

Picklands, J. (1975), Statistical inference using extreme order statistics, *Ann. Stat.*, *3*, 119–131.

R Development Core Team (2008), *R: A Language and Environment for Statistical Computing*, R Found. for Stat. Comput., Vienna, Austria. [Available at http://www.R-project.org.]

Rodgers, D. J., and K. A. Ryden (2001), Internal charging in space, in *Proceedings of 7th Spacecraft Charging technology Conference, Noordwijk, the Netherlands, 23–27 Apr., ESA SP-476*, edited by R. A. Harris, p. 25, Eur. Space Agency, Paris.

Rodgers, D. J., K. A. Hunter, and G. L. Wrenn (2003), The FLUMIC electron environment model, paper presented at 8th Spacecraft Charging Technology Conference, Huntsville, Alabama, 20–24 Oct.

Ryden, K. A., H. Jolly, A. Frydland, and P. Morris (1999), A compact electrostatic charging monitor for spacecraft, paper presented at 5th European Conference on Radiation and its Effects on Components and Systems (RADECS–99), pp. 120–125, Fontevraud, France, 13–17 Sep., doi:10.1109/RADECS.1999.858559.

Ryden, K. A., et al. (2008), Observations of internal charging currents in medium Earth orbit, *IEEE Trans. Plasma Sci.*, *36*(5), 2473–2481.

Ryden, K. A., A. D. P. Hands, C. I. Underwood, and D. Rodgers (2015), Internal charging measurements in medium Earth orbit using the SURF sensor: 2005–2014, *IEEE Trans. Plasma Sci.*, *43*(9), 3014–3020.

Taylor, B., C. I. Underwood, K. A. Ryden, and P. A. Morris (2009), A GIOVE derived Galileo electron spectrum and comparison to models, *IEEE Trans. Nuclear Sci.*, *56*(6), 3423–3428.

Vette, J. (1991), The AE-8 trapped electron model environment, *NSSDC Rep. 91-24*, Goddard Space Flight Cent., Greenbelt, Md.

Wrenn, G. L. (1995), Conclusive evidence for internal dielectric charging anomalies on geosynchronous communications spacecraft, *J. Spacecr. Rockets*, *32*, 514–520.

Wrenn, G. L., D. J. Rodgers, and P. Buehler (2000), Modelling the outer belt enhancements of penetrating electrons, *J. Spacecr. Rockets*, *37*, 408–415.

Wrenn, G. L., D. J. Rodgers, and K. A. Ryden (2002), A solar cycle of spacecraft anomalies due to internal charging, *Ann. Geophys.*, *20*, 953–956.